Wind Turbine Aerodynamics Using an Incompressible Overset Grid Method

Zahle, Frederik; Johansen, Jeppe; Sørensen, Niels

Published in:
Proceedings of The European Wind Energy Conference and Exhibition, EWEC 2007

Publication date:
2007

Document Version
Publisher's PDF, also known as Version of record

ewec 2007 MILAN

Europe's premier wind energy event

Organised by:

EWEA

THE EUROPEAN WIND ENERGY ASSOCIATION

25 YEARS POWERING CHANGE

Scientific proceedings

Milano Convention Centre,
Milan, Italy

7-10 May 2007

www.ewec2007.info

Supporting Organisations

European Commission

Ministry for the Environment Land and Sea of Italy

Intelligent Energy Europe

Intelligent Energy Europe

Associazione Nazionale Energia del Vento

Eolica Expo Mediterranean

Associazione Produttori Energia da Fonti Rinnovabili

Global Wind Energy Council

European Academy of Wind Energy

ewec 2007
MILAN
Europe's premier wind energy event

Scientific proceedings

Wind Turbine Aerodynamics Using an Incompressible Overset Grid Method

Frederik Zahle*, Jeppe Johansen*, Niels N. Sørensen*†
*Wind Energy Department, Risø National Laboratory, DK-4000 Roskilde, Denmark
†Department of Civil Engineering, Aalborg University, DK-9000 Aalborg, Denmark
frederik.zahle@risoe.dk

Abstract

In this paper 3D Navier-Stokes simulations of the unsteady flow over the NREL Phase VI turbine are presented. The computations are carried out using the structured grid, incompressible, finite volume flow solver EllipSys3D, which has been extended to include the use of overset grids. Computations are presented, firstly, on an isolated rotor, and secondly, on the downwind configuration of the turbine, which includes modelling of the rotor, tower and tunnel floor boundary.

The solver successfully captures the unsteady interaction between the rotor blades and the tower wake, and the computations are in good agreement with the experimental data available. The interaction between the rotor and the tower induces significant increases in the transient loads on the blades and is characterised by an instant unloading and subsequent reloading of the blade, associated with the velocity deficit in the wake, combined with the interaction with the shed vortices, which causes a strongly time varying response. Finally, the results show that the rotor has a strong effect on the tower shedding frequency, causing under certain flow conditions vortex lock-in to take place on the upper part of the tower.

1 Introduction

The predominant configuration of modern wind turbines has for the past decades been the three-bladed upwind turbine. Another configuration which has received less attention is the downwind, teetered, two-bladed concept. It has the advantage that the flapwise deflection of the blades gives rise to an increase in tower clearance, which makes it possible to design more flexible and lighter blades than is possible on upwind machines. Another advantage is that the bending moment acting on the shaft can be greatly reduced with the addition of a teetering hinge. Additionally, the downwind configuration can be operated using a free-yawing concept due to the restoring yaw moment of the rotor thrust. One of the reasons why the downwind concept was abandoned was that several field tests showed that considerable low frequency noise was generated when the blades pass through the tower wake [16, 20, 31]. The large variation in the measured data was attributed to the interaction of the blades with the unsteady tower wake.

Most engineering models for tower shadow effects (see for example [19]) do not include the unsteady effects associated with the blade-wake interaction (BWI) where most notably blade-vortex interaction can contribute large fluctuations in the loads. Instead, the models typically consider the tower wake in a time-averaged sense, thus ignoring the unsteady shedding of vortices from the tower. It is therefore clear that there is a need to improve these models to take these effects into account.

In a recent work Madsen et al. [21] combined an unsteady CFD simulation of flow over an isolated cylinder with the aeroelastic code HAWC including a noise model and showed that it is indeed the unsteady forces on the blades resulting from interaction with the tower wake that cause large fluctuations in the noise from a downwind turbine, with up to 10 dB increases compared to a simulation using a time averaged tower wake. The highest levels of noise were observed when the blades interacted directly with the tower vortices. This result shows that not only is the unsteady nature of BWI important to the transient loads on a wind turbine, but it is also essential to include these when investigating the noise associated with this configuration. In this respect Computational Fluid Dynamics (CFD) can be a highly valuable tool, since it can provide insight into the physical phenomena underlying the dynamics of blade-wake interaction, which can subsequently be used to refine the empirical tower shadow models that are used in design codes.

The aerodynamics of isolated wind turbine rotors has been investigated extensively using Computational Fluid Dynamics (CFD) [see for example 7, 8, 14, 18, 22, 34, 41, 42]. These works showed that CFD tools are capable of accurately capturing the complex flow on wind turbine blades, in particular the complex three-dimensional features which dominate the flow at high loadings. Additionally, Duque et al. [8] modelled the flow around a complete wind turbine in a downwind configuration with rotor, tower and nacelle. However, due to computational issues, the unsteady interaction of the tower wake and the rotor was not fully captured. Xu [40] also shows results of rotor-tower interaction on the NREL Phase IV using an overset grid method. Due to a very coarse grid resolution around the tower, the unsteady nature of the tower wake was not captured.

In the in-house Navier-Stokes flow solver EllipSys3D [26, 27, 32] it has so far only been possible to compute the flow around an isolated rotor. The modelling of an entire wind turbine poses a number of challenges to the flow solver, most notably that the relative movement between the rotor and tower has to be handled in some appropriate manner. Recently, Zahle [43] extended the code such that this relative movement could be modelled directly providing the basis for simulating the unsteady flow over a complete wind turbine configuration including the rotor, tower, nacelle and ground boundary. The modelling of the relative movement of solid bodies can be achieved by means of a variety of methods. Through a preliminary literature study it was found that the overset grid method, also known as Chimera or composite grid method was the most flexible method to handle this problem, since it allows for grids to move virtually unrestricted relatively to each other. Additionally, the method also addresses the many limitations of structured grid generation, making it possible to create grids around complex geometries that traditionally has only been possible using unstructured grids. In [43] the rotor-tower interaction on the NREL Phase VI turbine was thus investigated using the new method and it was demonstrated that the EllipSys3D solver captured the unsteady interaction between the tower wake and the passing rotor blades. The present article is in part based on this work.

The NREL Unsteady Aerodynamics Experiment [9, 29] is to date the most extensive experiment on a wind turbine representative in size and flow regime of full-size wind turbines conducted under controlled inflow conditions. The experiment was carried out in the 24.4 m × 36.6 m NASA Ames wind tunnel on a two bladed 10 m diameter stall regulated wind turbine operating at 72 rpm. The rotor was mounted at a height of 12.2 m on a tower with a diameter of 0.4 m on the top section with a wider base of 0.6 m. The turbine could be operated in both an upwind and downwind configuration. In both configurations the rotor was mounted with a 1.4 m clearance to the tower, corresponding to 3.5 tower diameters. One blade was instrumented with pressure probes and pressure taps. The pressure taps were placed along the suction and pressure sides of the blade at five spanwise locations on the blade at r/R=0.3, 0.47, 0.63, 0.80 and 0.95. Additionally, five hole pressure probes were placed 80% chord upstream of the blade at r/R=0.34, 0.51, 0.67, 0.84 and 0.91 to measure the local flow angles.

In this paper results are presented from unsteady computations of the flow over the NREL turbine with focus on the downwind configuration. Firstly, simulations of the flow over an isolated rotor are presented to validate the overset grid method against the original solver and experimental results. Secondly, the flow over the downwind configuration of the turbine is presented. Through an analysis of the extracted blade forces and surface pressure distributions and visualisation of the flow field, a discussion on the interaction between the rotor and the tower will be made, aiming at identifying the key features of the interaction. It will be demonstrated that the newly developed overset grid version of EllipSys3D successfully captures the unsteady interaction between the rotor blades and the tower, and that the computations are in good agreement with the experimental data available from the NASA Ames experiment.

2 Computational Methods

2.1 Base Solver

For all computations the EllipSys3D pressure based incompressible Reynolds averaged Navier-Stokes flow solver written by Michelsen [26, 27] and Sørensen [32] is used. The code uses the finite volume method, solving for the primitive variables u, v, w, and p, in general curvilinear coordinates. The variables are stored in a collocated grid arrangement, and odd/even pressure decoupling is avoided using the Rhie-Chow interpolation [28]. The iterative SIMPLE or PISO algorithm is used to advance the solution in time using a second-order accurate scheme. The convective terms are discretised using either the second order upwind difference scheme, SUDS, or the Quadratic Upstream Interpolation for Convective Kinematics Scheme, QUICK, and the viscous terms are discretised using the central difference scheme. The momentum equations are solved decoupled from each other using a red/black Gauss-Seidel point solver. To accelerate the convergence of the pressure-correction equation a multigrid solution strategy is implemented combined with the additive Schwarz method, where

each sub-domain is solved for simultaneously.

The code is fully parallelised using the MPI library with a multiblock decomposition of the solution domain. The block-block communication is done through one layer of ghost cells around each block. The cell vertices are required to coincide on interfaces such that conservation can be maintained.

For computations of flow over aerofoils and wind turbine blades the EllipSys3D code uses the $k-\omega$ SST model by Menter [25], because of its good performance in wall bounded adverse pressure gradient flows.

2.2 The Overset Grid Method

The overset grid method, also known as chimera or composite grid method, addresses many of the limitations of traditional structured grid methods, while at the same time maintaining their advantages such as solution strategies and parallelisation. The method allows for the decomposition of the problem into a number of simpler grids, which overlap each other arbitrarily. If dealing with a multibody problem, appropriate body-fitted grids can be generated around each component, making it possible to model virtually any configuration. Since each body grid is independent of the other grids, problems involving relative movement of bodies are naturally handled.

Important flow features can be resolved by refined Cartesian meshes, which together with the body fitted meshes can be embedded in Cartesian background meshes that are successively coarsened towards the farfield where there is no need for high resolution of flow features. To accommodate the solid bodies and Cartesian refined grids, cells are removed from the background grids where necessary.

Among the first to work with this type of solution methods were Atta [1], Steger et al. [35] and Benek et al. [3], the latter starting the development of the well-known OVERFLOW code, later adapted for moving grid problems by Meakin [23, 24]. For incompressible flow applications a number of overset grid methods have been developed, see for example [5, 6, 10, 11, 12, 36, 37, 38, 44].

In the present implementation by Zahle [43] each group of simply connected blocks is solved using boundary conditions on the overlapping interfaces based on interpolated values of velocity from neighbouring grids using trilinear interpolation. Two layers of fringe cells are used such that second order accuracy can be maintained across interfaces. Since this interpolation is non-conservative, the lack of conservation of the integral quantities must be addressed. An explicit correction of the conservation error is implemented, since a divergence free field is required to solve the pressure-correction equation. The correction is placed in internal cells along the overset boundaries and is distributed proportionally to the local mass flux. As stated above only velocities are interpolated, since interpolation of velocities and pressure would lead to an ill-posed problem. The solution of the pressure is thus obtained on the basis of the mass fluxes calculated from the momentum equations.

The additional cost associated with the overset grid method is caused by the need for determining the connectivity between each block group. For each fringe cell along the overset interfaces appropriate donors must be identified that can supply the boundary conditions. This process can be quite costly, and since it must be carried out at each time step in a moving grid simulation it has to be parallelised. In EllipSys3D the connectivity routines are thus fully parallelised and apply a stencil jumping technique to locate cells together with the nth-level restart method [2] to guess the identity of processors that hold valid donors for each fringe cell. Likewise, the communication of flow field data must be carried out in a parallel manner. To minimise communication latency non-blocking MPI calls are used to transfer information between individual processors.

The $k-\omega$ SST model has not yet been implemented for use on overset grids, since it requires the specification of two zonal functions that are computationally heavy to evaluate on moving overset grids. As such, only the original $k-\omega$ model can be used.

For further details on the numerical implementation see [43].

3 Computational Meshes

In the present study curvilinear grids are used around the two-bladed rotor and the tower, while Cartesian background grids are used to cover the remainder of the domain. The advantage of this approach is that the grid can more easily be designed to resolve regions of high flow gradients in the vicinity of the rotor and tower, without carrying the clustering of cells to the farfield. This coarsening strategy reduces the waste of cells in the farfield typically seen with O-grid or C-grid configurations.

Two different grids were made: Firstly, a reference mesh containing only the rotor, N1, was made, where the farfield side boundaries were 4.5 rotor diameters away from the centre of rotation. The inlet was placed 4 rotor diameters upstream of the rotor, and the outlet was 8 diameters downsteam. The rotor mesh, which was generated using HypGrid [33], consisted of 40 blocks of 32×32 cells to cover the surface of the two blades with 256 cells in the chord-wise direction, 64 cells in the spanwise direction, and four blocks of 32×32 to cover each blade tip. The grid was grown out approximately 1 m from the surface with a total of 64 cells in the normal direction stretched using a tangent hyperbolic function. The height of the first cell in the boundary layer was 1×10^{-5} m corresponding to y^+ values of less than 2. This grid was embedded in three Cartesian meshes, successively coarsened towards the farfield consisting of 36, 27, and 12 blocks of 33^3 cells, respectively. The total number of cells in the grid was 5.57M cells. The boundary conditions consisted of an inlet with a prescribed velocity, an outlet with a zero gradient condition, and cyclic boundary conditions on the other four boundaries. On the surface of the blades a no-slip condition was prescribed. The mesh is shown in Figure 1.

The geometry of the Phase VI turbine has been somewhat simplified. In the computational model the tower has a constant diameter of 0.4 m along the entire height of the tower which differs from the actual geometry which has a wider base. Additionally, the nacelle has been omitted since it would require a considerable amount of cells to properly resolve its geometry. Although it is likely to have a strong influence on the flow-field in the root section of the blade, its influence was thought to be less pronounced on the outboard sections of the blade. The rotor was modelled without coning and teeter, whereas in fact the Phase VI turbine in its downwind configuration was run with a cone angle of 3.4° and a teeter angle which on average was 3°. The combination of teeter and coning, however, results in the blades being approximately parallel to the tower axis during the tower passage which justifies the above simplification.

The computational mesh for the rotor-tower configuration consisted of five individual block groups: two curvilinear for the rotor and tower and three Cartesian which were successively coarsened towards the farfield (See Figure 2). The rotor mesh was identical to that used in the rotor-only mesh. The tower mesh consisted of 128 cells around the cylinder and 384 cells in the vertical direction and one grid of 32×32 to cover the rounded free end. The mesh was grown out 1 m in the normal direction using 32 cells totalling 13 blocks of 32^3. The height of the first cell was 1×10^{-4}m.

The cross sectional dimesions of the domain were equal to those of the NASA Ames wind tunnel, 24.4m $\times$ 36.6m. The domain was 80 m long with the turbine placed 20 m downstream from the inlet. The bottom boundary was prescribed as a no-slip wall, whereas the three other side walls of the tunnel were modelled using symmetry boundary conditions. A standard inlet condition with a given velocity was prescribed at the inlet, and a zero gradient condition was specified on the outlet. To capture the ground shear layer reasonably well, the three Cartesian groups and the tower grid had a first cell height of 1×10^{-4} m. The inner Cartesian block group had physical dimensions 14 m $\times$19 m $\times$ 14 m and consisted of $160 \times 192 \times 128$ cells in the x, y and z directions, respectively. The mesh was made finer in the rotor plane to match the grid dimensions of the rotor grid to properly resolve the tip vortex from the rotor. The middle Cartesian block group had physical dimensions 20 m$\times$ 22.5 m $\times$ 25 m and contained $96 \times 128 \times 96$ cells. The outer block group had the dimensions of the tunnel 24.4 m $\times$ 36.6 m and consisted of $64 \times 97 \times 97$ cells. The total number of cells in the grid was 9.6M cells. This grid will be referred to as grid N2. The grid assembly is shown in Figures 2, 3 and 4.

4 Computational Framework

The computations were all carried out using the SUDS scheme to discretise the convective terms while the PISO algorithm was used to solve the coupled velocity/pressure equations. Due to the uncertainties associated with the limited implementation of the $k-\omega$ SST model the computations were all carried out using the original $k-\omega$ model by Wilcox [39]. As such, the flow was assumed to be fully turbulent.

From previous experience with the non-overset version of the code it was found that approximately 800 iterations per revolution was needed to obtain an accurate solution of the integral forces on the NREL blade. To speed up the convergence of the solution, the computations were started up at a coarse time step of $dt = 2 \times 10^{-3}$ and run until the flow was sufficiently developed. This was necessary due to the long time required for the unsteady tower wake to develop fully. Once the wake had developed, the computations were restarted at a finer time step of $dt = 1 \times 10^{-3}$. With a rotational frequency of 72 RPM, this corresponded to a time resolution of 0.43° per time step.

4.1 Computational Cost

All computations presented in this work were computed on the Risø Central Computer Facility, "Mary" [17] which consists of 240 Dell PowerEdge 750 nodes, each equipped with single processor Intel Pentium 4 (Prescott) 3.2 GHz CPUs and 1 MB cache. Each ma-

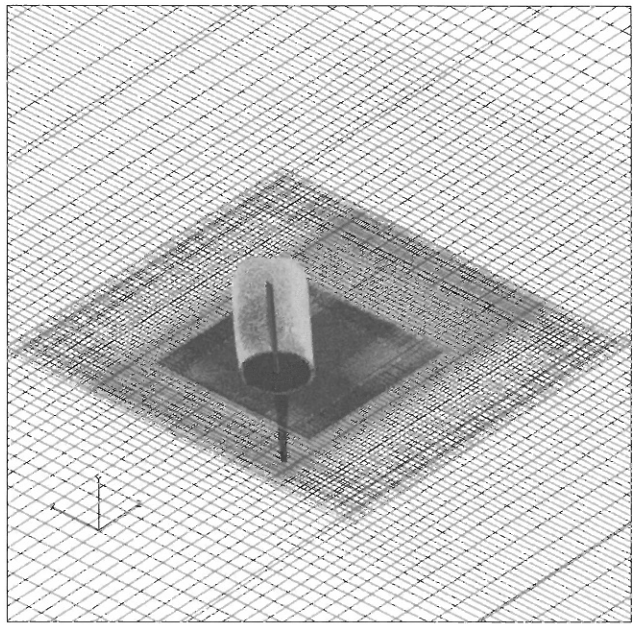

Figure 1: Mesh for the rotor-only configuration.

chine has 2 GB of memory. The nodes are connected by Gigabit Ethernet by means of a system of D-Link switches.

Table 1 shows the computational time per iteration for the two main overset routines and the total computational time. The Copy3DOG routine carries out all communication of flow field data locally on each processor as well as the parallel communication between processors. The ConnectOG routine sets up the connectivity information for the overset grid system and is called at every time step to re-establish the connectivity between the grids with relative movement. As can be seen the overset routines occupy approximately 50% of the total computational time. This is mainly due to the high cost associated with the connectivity routine. The solver is seen to scale very well when increasing the number of processors from 45 to 67. The fact that the Copy3DOG routine appears to exhibit super scaling is purely related to the distribution of blocks on the processors, which cause large imbalances between the nodes, which will vary according to the number of processors used.

Prc's	Copy3DOG	%	ConnectOG	%	Total
45	30.5	23.5	41.6	32.0	129.8
67	11.5	13.9	23.6	28.6	82.5

Table 1: Computational cost (wall-clock time in seconds) per iteration of the rotor-tower problem.

5 Isolated Rotor Computation

Computations of flow over the isolated NREL Phase VI rotor have previously been carried out using ElipSys3D [34]. To validate the overset grid method, equivalent overset computations were carried out and compared to these results as well as the experiment. The upwind 7 m/s case with no teeter (Sequence H) was chosen for the comparison.

The overset computations were carried out using

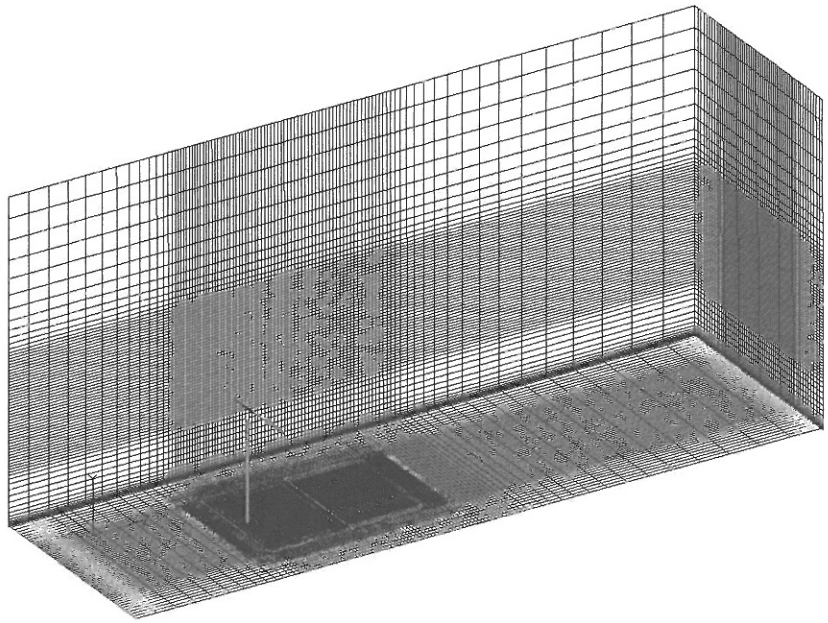

Figure 2: Mesh for the rotor-tower configuration.

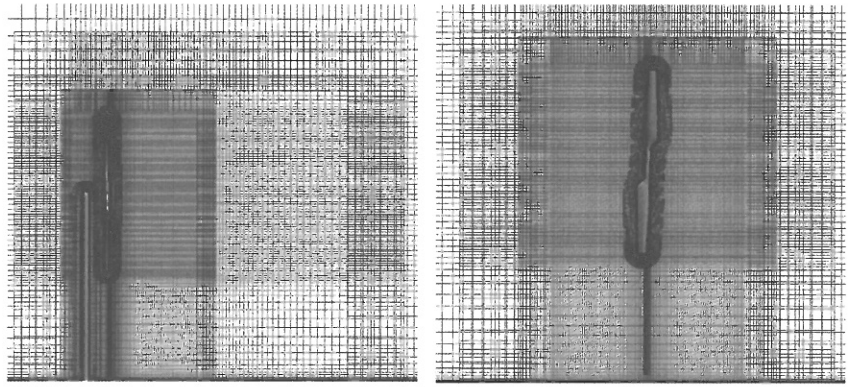

Figure 3: Side and back view of the mesh system for the rotor-tower configuration.

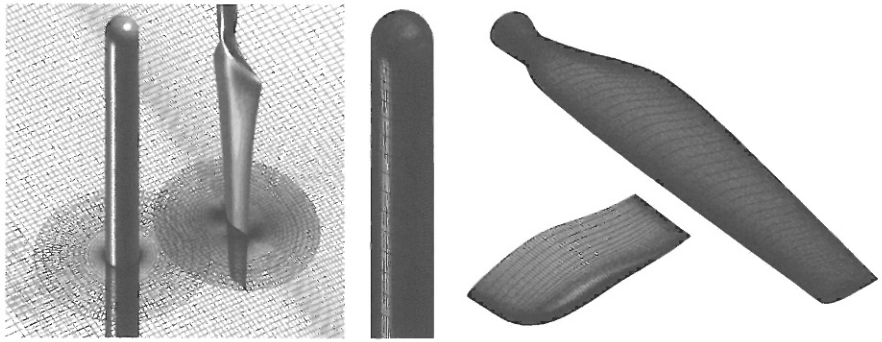

Figure 4: Detail of the rotor and tower grids.

grid N1 which was presented in detail in Section 3. To reduce the computational cost the simulation was carried out as an unsteady moving grid simulation without any relative movement between the rotor grid and the background Cartesian grids. The computations were otherwise carried out using the solver options described in Section 4. For the non-overset computations the solver parameters were identical to the overset ones, except that the $k-\omega$ SST turbulence model was used. However, this was expected not to cause any significant differences in the results, since the flow ove the blades at 7 m/s is predominantly attached.

Figure 5 shows the normal and tangential force coefficients along the blade computed at five spanwise locations corresponding to the pressure tap locations in the experiment. Although the results differ slightly from the experimental results the overall agreement is very good. There is also some discrepancy between the overset and non-overset computations. This, however, can most likely be explained by slight differences in the cell distribution in the normal direction of the rotor grid, as well as the fundamentally different mesh topology in the off-body grids, which will affect the development of the wake.

Figure 6 shows the pressure coefficient distributions at five spanwise locations on the blade for the overset computations compared to the non-overset computations and experimental results. The agreement is very good between the two computations and the experiment, with only slight differences at the outermost spanwise location.

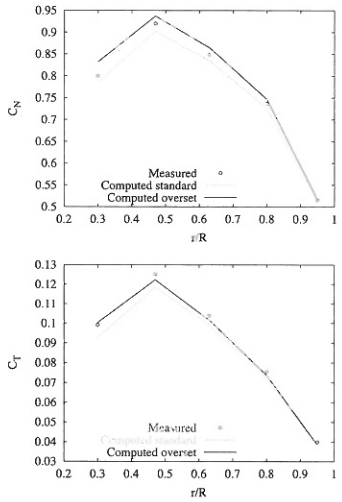

Figure 5: Normal and tangential force coefficients for a wind speed of 7 m/s for the isolated rotor.

6 Rotor-Tower Computations

Three cases from Sequence B in the Unsteady Aerodynamics Experiment were chosen where the nominal inflow velocities were equal to 7.0 m/s, 10 m/s, and 15 m/s. However, due to wind tunnel anomalies the actual inflow velocities were 6.7 m/s, 10.3 m/s, and 15.2 m/s.

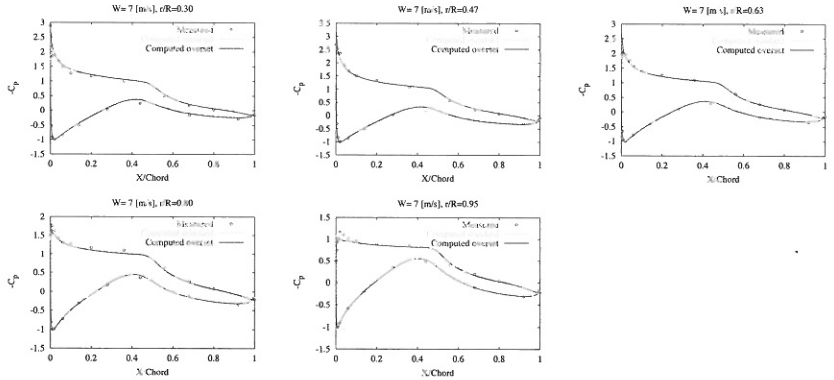

Figure 6: Pressure distribution coefficients for a wind speed of 7 m/s for the isolated rotor.

The computational results are analysed by firstly presenting the extracted flow field data, where the key features of the flow will be identified; secondly, the response of the blades to the wake interaction are compared to the experiment. Finally, the response of the tower to the interaction is analysed.

Surface pressures and skin friction were extracted on both blades in the same radial positions as in the experiment (30%, 47%, 63%, 80%, and 95% span). Additionally, surface pressures were extracted on the tower at eight heights, five within the rotor radius and three below. Force coefficients were computed from the integrated pressure and skin friction coefficients. The entire flow field was exported every 30° azimuth for visualisation purposes. In the remainder of this paper the two blades will be referred to as *blade 1* and *blade 2*.

6.1 Flow Field

Figure 7 shows the flow field surrounding the turbine using an iso-surface plot of vorticity magnitude. The mesh is also shown in the plot with grid interfaces highlighted green. The unsteady vortex shedding from the tower is clearly visible, and it can be seen that the vortex street is quite coherent and well-preserved approximately 10 m downstream. The root and tip vortices from the rotor are clearly visible and likewise preserved well for approximately 10 m downstream. The dissipation of the vortices does not appear to be linked to the presence of overset interfaces, but rather to the stretching of the grid. The rotor has a visibly strong influence on the tower shedding, causing a difference in shedding frequency on the upper and lower parts of the tower. This results in a dislocation with two distinct shedding cells separated by a disorganised region approximately 1 m below the rotor disc.

The flow is further illustrated in Figure 8 which shows the flow field at a vertical cut plane of x=0 bisecting the turbine, at an instant where the blades are aligned vertically with the tower. From this plot it is again evident that the vortex street is convected downstream at a different velocity on the upper and lower parts of the tower. It also appears as if the blade tip vortices cause the tower vortices to wrap up around the blade vortices enhancing the stretching of the tower vortices.

Figures 9 and 10 show a sequence of snapshots of the flow field for two blade vortex encounters for the low wind case at W=6.7 m/s. In Figure 9 a vortex of negative vorticity convects through the rotor plane that the blade in this case encounters virtually head-on. The direct encounter between the blade and the vortex causes the vortex to be split into two fragments, one small fragment upstream of the blade wake and another one downstream which has been stretched considerably by the passing blade. This BVI event will be referred to in the remainder of this paper as a *type 1* passage.

In Figure 10 the blade encounters a vortex of positive vorticity which is located slightly more upstream than in the previous event. Again the vortex is divided in two fragments, one small fragment downstream of the blade wake and a more stretched fragment upstream. This situation will be referred to as

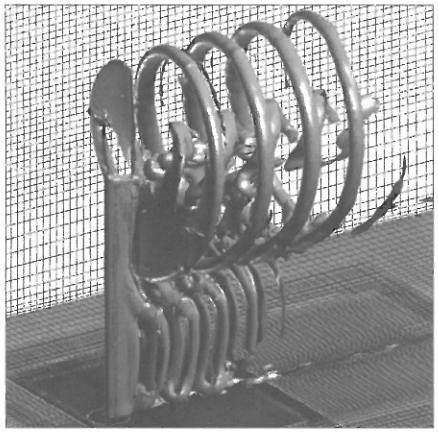

Figure 7: Iso-vorticity plot of the instantaneous flow over the turbine for a wind speed of 6.7 m/s.

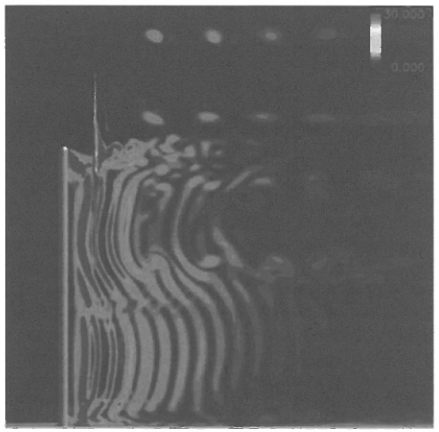

Figure 8: Vorticity magnitude contour plot of the instantaneous flow over the turbine for a wind speed of 6.7 m/s.

a *type 2* passage. These plots also highlight the large difference between the blade velocity and the vortex convection velocity which characterises the interaction taking place on the outer parts of the blade. On the inner parts of the blade, however, the blade velocity is much lower, therefore decreasing the relative velocity difference between the blade and the vortex. An analysis of the blade forces associated with these interaction events will be presented in the subsequent sections of the paper.

A horisontal coordinate surface of the mesh is also shown on the plots to highlight the location of the overset interfaces. It is evident that the flow features are transported smoothly across the overset interfaces despite the relatively coarse mesh used to resolve the tower wake.

6.2 Blade Response

In this section the effects of the rotor-tower interaction on the blade responses will be analysed. This is done by firstly presenting the integral normal force coefficients at the five spanwise sections on the two blades, followed by a presentation of the responses at the 80% span section for one inflow velocity, where the moment coefficients and pressure distributions are presented. Additionally, the computed results are compared with the experiment.

6.2.1 Normal Force Coefficient

The normal force acting on the blades are plotted in Figures 11 to 13 for the five spanwise sections for the three wind speeds, where three consecutive revolutions from the computations are superimposed on each other and compared to the experimental data as a function of blade azimuth. The experimental data set consists of 35 consecutive revolutions that are plotted together with the azimuthal average.

From the computations it is evident that the character of the blade responses differs significantly for the three flow cases. At w=6.7 m/s (Figure 11) the response to the tower wake interaction is on the outer parts of the blades limited to a fairly small fraction of the blade cycle with a small recovery period. At the higher wind speed of w=10.3 m/s (Figure 12) the transient recovery covers a greater portion of the blade cycle. The recovery is characterised by an initial increase in C_N followed by a slight decrease and a slow climb to the free stream level. At w=15.2 m/s (Figure 13) this transient recovery is considerably more pronounced with a large overshoot and subsequent drop in C_N which covers most parts of the blade cycle.

The blade responses vary significantly depending on the exact nature of the BVI event. Two such events are illustrated in Figures 9 and 10 for the low

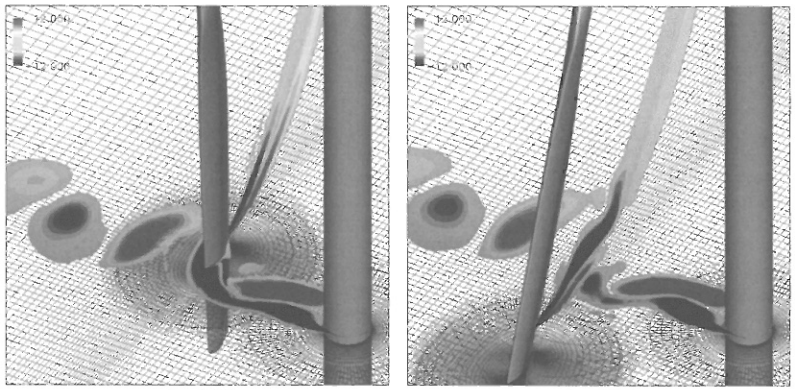

$\psi = 177°$ $\psi = 207°$

Figure 9: Vorticity contour plot of a *type 1* passage at w=6.7 m/s showing an encounter with a vortex of negative vorticity (clockwise rotation). The vorticity contours are plotted on a plane of constant radius of 4.02 m corresponding to 80 % span.

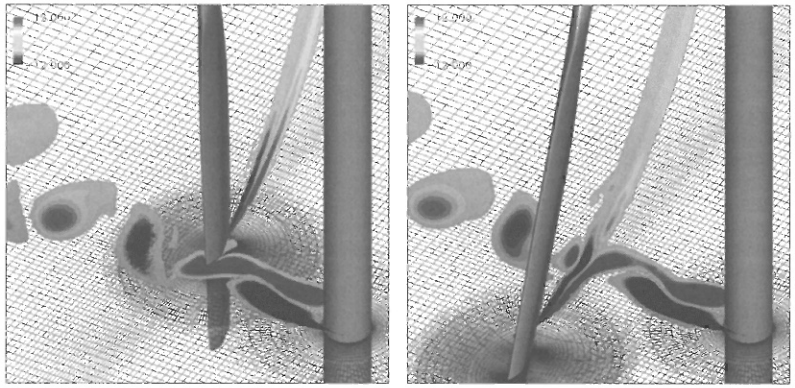

$\psi = 177°$ $\psi = 207°$

Figure 10: Vorticity contour plot of a *type 2* passage at w=6.7 m/s - showing an encounter with a vortex of positive vorticity (counter-clockwise rotation). The vorticity contours are plotted on a plane of constant radius of 4.02 m corresponding to 80 % span.

wind case at w=6.7 m/s which give rise to the responses illustrated in Figure 11. A blade-vortex encounter clearly causes different responses depending on the sense of rotation of the vortex. In the type 1 encounter characteristic of blade 1 the blade encounters a vortex of negative vorticity as it exits the wake which appears not to generate as significant a fluctuation in the response as a type 2 encounter where the blade encounters a vortex as it enters the wake.

The blade responses at w=6.7 m/s and w=15.2 m/s enter a seemingly periodic state with very little variation between consecutive passages, whereas there is greater variation for the w=10.3 m/s case. This somewhat surprising periodicity of the blade re-

sponses was found to be directly linked to the vortex shedding from the tower and will be analysed further in a later discussion.

Comparing the computed normal forces to the measurements it can in Figures 11 to 13 be seen that the agreement is best at the lowest wind speed. The freestream level of the normal force is in good agreement with the experiment, best on the middle sections of the blade where the flow is mostly two-dimensional, whereas on the inner and outer parts of the blade where three-dimensional effects are dominant, the agreement is slightly poorer. Additionally, the fact that the nacelle is not modelled in the computations could influence the accuracy of the computations on the inner parts of the blade. At the three middle sections of the blade the responses in the tower shadow region all fall within the experimental spread. At w=10.3 m/s the agreement is poorer with a consistent overestimation of the normal force on the outer four sections. Likewise, at w=15.2 m/s the agreement in the freestream level is less favourable than at low wind. However, the magnitude and character of the blade response during the tower wake interaction is captured well in all three cases. At 15.2 m/s the pronounced transient peak in the response during the recovery is captured well, although the recovery time is slightly longer in the computation.

6.2.2 Moment and Surface Pressure Coefficients

Figures 14 and 15 show plots of the normal force and moment coefficients for the low wind case of w=6.7 m/s. These are accompanied by time history plots of the surface pressures on the blade during the tower passage shown in Figures 16 and 17. The crosses on the normal force and moment coefficient curves correspond to the flow field snap shots shown in Figures 9 and 10. Interaction events similar to the ones observed in the computations were identified from the experimental data and are also plotted in Figures 14 and 15.

The quarter chord moment acting on the blades is critically dependent on the state of the tower wake. In the present flow case one blade experiences an overall decrease in pitching moment during the BWI whereas the other blade experiences a sharp increase. This strongly suggests that the interaction of the blade with the tower wake introduces local changes in the pressure distribution which alters the moment acting on the blade beyond those associated with changes in inflow angle. In Figure 16 it can be seen that in addition to the reduction in incidence associated with the velocity deficit, the interaction with the vortex seems to cause a complete collapse of the suction

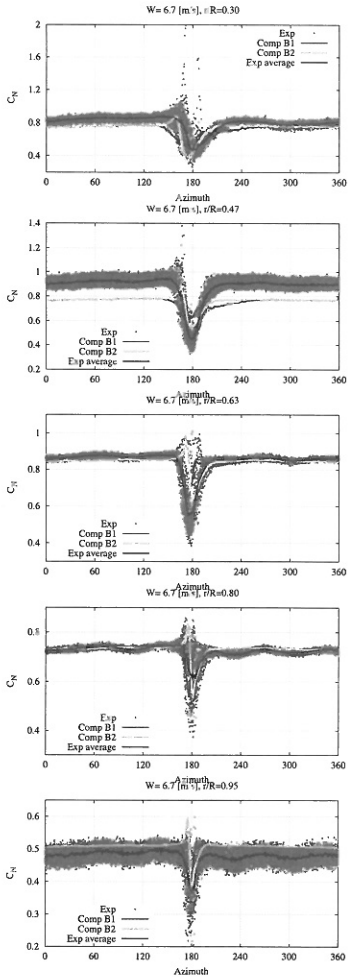

Figure 11: Normal force coefficient on blades 1 and 2 for three consecutive revolutions at w=6.7 m/s compared to experimental results.

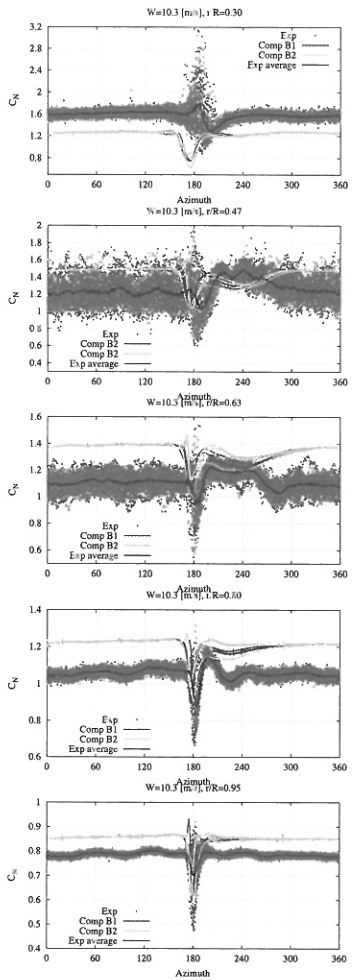

Figure 12: Normal force coefficient on blades 1 and 2 for three consecutive revolutions at w=10.3 m/s compared to experimental results.

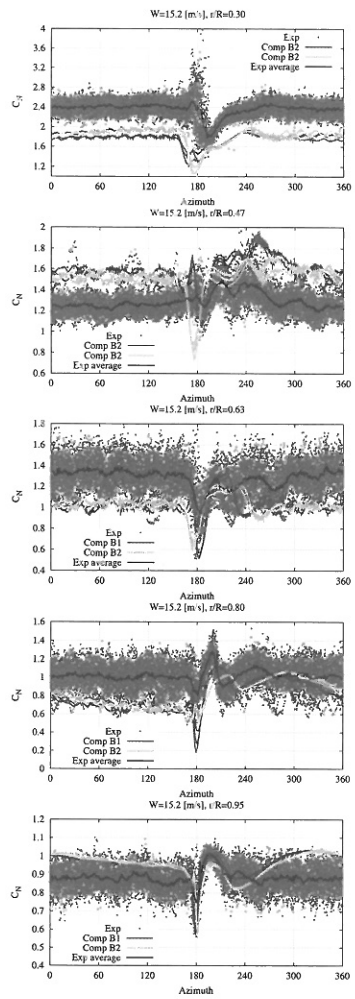

Figure 13: Normal force coefficient on blades 1 and 2 for three consecutive revolutions at w=15.2 m/s compared to experimental results.

peak, which results in a nose down pitching moment corresponding to point C in Figure 14. As the blade exits the wake the suction peak recovers which increases the nose up moment. The events marked D and E could be associated with the slight changes in the trailing edge suction which are visible in Figure 16 caused by interaction with a second tower vortex and the shedding of bound vorticity from the blade.

As shown in Figure 10 blade 2 encounters a vortex of positive vorticity (type 2). The induced velocity from the vortex causes an increase in loading on the blade, most visible on the leading edge. The encounter with the vortex does not cause in this case a complete collapse of the suction peak as was seen on blade 1. As the blade passes the vortex and experiences a decrease in flow angle the moment decreases momentarily before increasing drastically reaching a maximum at point C. It is likely that this large increase in the moment is caused by an increase in suction on the pressure side associated with the interaction with the vortex shed from the tower. This is followed by a rapid decrease in the moment as the vortex convects past the trailing edge, which at point D causes a small wiggle in the moment curve as is visible in Figure 16. As the blade incidence increases, the moment recovers steadily to the freestream level. Event E could as for blade 1 be associated with the shedding of bound vorticity.

As shown in Figure 14 a type 1 BWI event does in the experiment also produce a nose down moment with a minimum at the point where the C_N curve reaches its minimum. The type 2 BWI event (Figure 15), does in the experiment also produce a strong nose up moment which has a maximum at the point where the C_N curve reaches its minimum. It also seems that the subsequent recovery as the blade exits the wake is in good agreement. The fact that isolated passages from the experiment are in such surprisingly good agreement with the computations suggests that the simulations capture the detailed physics underlying the interaction between the rotor and the tower wake.

6.3 Tower Response

For two of the flow cases in the present study the responses of the blades entered a periodic state. This suggests that the shedding frequency of the tower was in phase with the blade passage frequency. However, in a computation of the flow over an isolated tower at w=6.7 m/s the shedding frequency was found to be 4.1Hz, which is not equal to or a multiple of the rotational frequency of 1.2 Hz (1P) (see [43]).

This indicates that the tower shedding was modified strongly by the presence of the rotor. Indeed, this is the case as illustrated in Figure 18 where the side force on the tower is plotted at the same vertical positions as the blade pressure tap positions for the three wind speeds. The shedding pattern within the rotor radius is strongly affected by the blade passages which cause the shedding to become irregular and asymmetric. For the low wind case the vortex shedding is clearly periodic with three shedding periods per revolution. As can be seen, the shedding is strongly correlated along the span of the tower. The shedding strength is amplified significantly which appears to be strongest on one side of the tower with peak amplitudes of up to 0.24. On the lower part of the tower, however, the shedding frequency is higher at 4.1 Hz, equal to that found on the isolated tower giving a Strouhal number of 0.24. The rotor thus causes a 12% shift of the shedding frequency on the part of the tower within the rotor disc compared to the shedding frequency on the lower part. As was previously pointed out, this change gives rise to a dislocation of the vortex street below the rotor disc as shown in Figures 7 and 8. At w=10.3 m/s there seems to be no correlation of the shedding frequency with the rotational frequency. Averaged over 6 revolutions the shedding frequency inside the rotor disc was 5.6 Hz whereas outside the rotor disc it was 6.0 Hz corresponding to a Strouhal number of 0.23. This corresponds to a 6.6 % shift of the shedding frequency inside the rotor disc. There was indication that the shedding frequency entered a 2P periodic state, however, the simulation time was not sufficiently long to confirm this. At w=15.2 m/s the tower shedding again enters a 1P periodic state with seven vortex shedding cycles per revolution. Outside the rotor disc the shedding frequency was equal to 8.79 Hz equivalent to a Strouhal number of 0.23. This results in a 4.6 % change in the shedding frequency inside the rotor disc.

7 Discussion

The dynamic response of a blade in an unsteady flow is commonly associated with the so-called reduced frequency $k = \frac{c\omega}{2U_{rel}}$, where c is the local chord length, ω is some characteristic frequency, and U_{rel} is the relative velocity seen by the blade. In the case of blade wake interaction the characteristic frequency will be proportional to the time spent in the unsteady wake of a given span section. The time spent in the wake is related to the tower wake width and the local blade section chord length, such that the root sections of the blade will subtend a larger azimuthal range than the outer sections, increasing the effective time spent

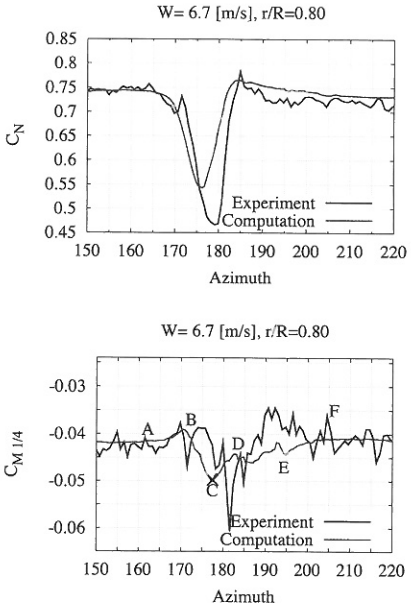

Figure 14: Detail of normal force and moment coefficients on blade 1 at 80% span at w=6.7 m/s.

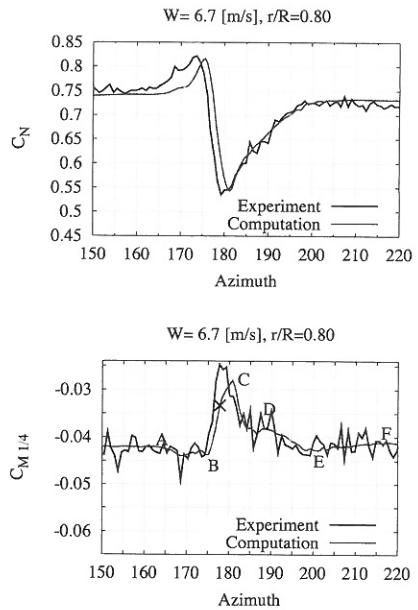

Figure 15: Detail of normal force and moment coefficients on blade 2 at 80% span at w=6.7 m/s.

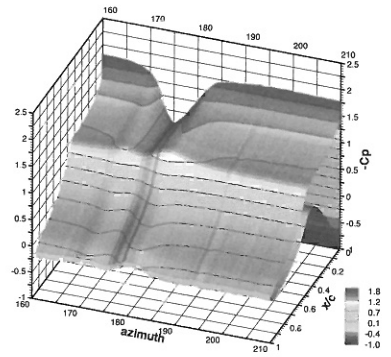

Figure 16: Time history of the surface pressure coefficients on blade 1 at 80% span at w=6.7 m/s.

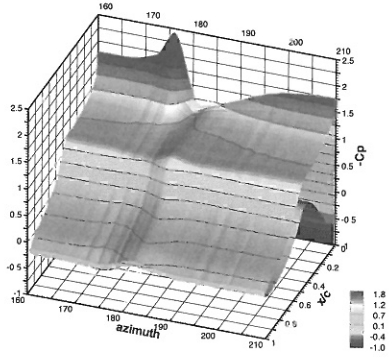

Figure 17: Time history of the surface pressure coefficients on blade 2 at 80% span at w=6.7 m/s.

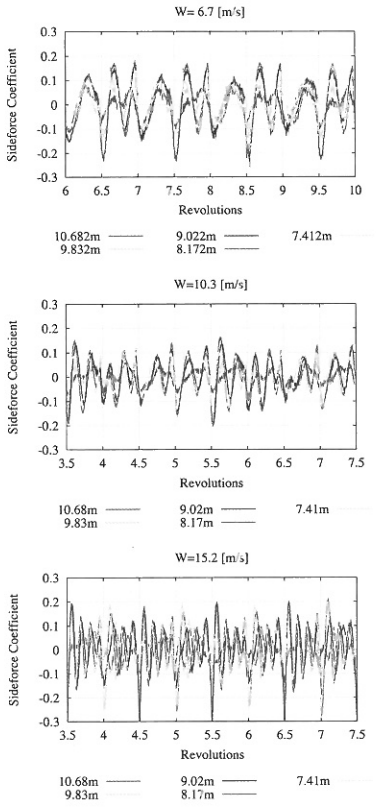

Figure 18: Time history of the tower side force coefficient for wind speeds w=6.7 m/s, w=10.3 m/s and w=15.2 m/s at the equivalent heights of the five blade pressure tap stations. Blade passages take place every half revolution.

in wake conditions. Taking the w=6.7 m/s case, at the 34% section the time spent in the wake was 0.22 s with the wake effect subtending 95° azimuth, resulting in a characteristic frequency of $\omega = 4.6\ s^{-1}$. At the 84% section the wake effect subtended 32° azimuth such that the time spent in the wake was 0.073 s, yielding a characteristic frequency $\omega = 17.29\ s^{-1}$. This results in a reduced frequency of $k = 0.123$ on the inner part of the blade and $k = 0.100$ on the outer part. This would suggest that effects such as phase-shifts/time delays in the blade response can be significant during a BWI event. Although the relative blade velocities increase significantly towards the tip, the effective reduced frequency is fairly constant along the span of the blade since the velocities are balanced by the increased time scales associated with the BWI towards the root. As such - for the present wind turbine - effects of phase-shifts should not vary significantly along the span of the blade on account of the reduced frequency.

A much more dominant factor seems to be the local blade loading. On a stall regulated wind turbine the angle of attack will vary according to the wind speed. In [13] Johansen and Sørensen derive the 3D $C_l - \alpha$ curves for the NREL Phase VI blade, which are shown to differ significantly along the span. At the inboard sections of the blade the lift reaches high values that persists at large incidences, which is caused by a so-called radial pumping of the separated boundary layer. Towards the middle sections of the blade the 3D lift curve resembles more the 2D lift curve, whereas 3D effects in the tip region cause a reduction in the lift. Both the experiment and computations show that the angle of attack of the blade has a large influence on the aerodynamic response of the blade as it passes through the tower wake as well as during the recovery. The response at a given blade section clearly depend critically on where on the $C_l - \alpha$ curve it operates. The largest differences in the response were observed during the recovery period where significant hysteresis effects were observed at high wind speeds.

Figure 19 shows instantaneous snap shots of the surface restricted streamlines on the suction side of the blade at 90° azimuth. Trailing edge separation is evident over a large portion of the blade for a wind speed of 10 m/s with a high degree of three-dimensional radial flow resulting from the rotational effects. At 15 m/s most of the flow over the blade is separated with only a small portion of attached flow on the outer 15% of the blade. The surface restricted streamlines suggest the presence of a vortical flow structure around the 30% span section.

In the 7 m/s case (Figure 11) the influence of the BWI covers a fairly narrow azimuth range on the outer sections of the blade. At this wind speed the blade operates in the pre-stalled region where the dynamic response is mostly linear with a rapid recovery when exiting the wake. Blade-vortex interaction (BVI) events appear to cause significant peaks in the normal force. On the inner sections the recovery is for blade 1 much slower than for blade 2. This could be

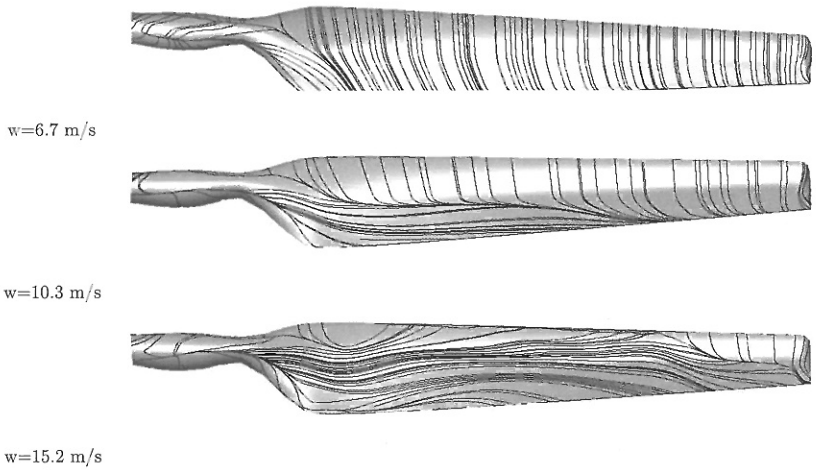

Figure 19: Instantaneous surface restricted streamlines on the blade suction side at $\psi = 90°$ for the three computed cases.

related to some characteristic frequency of the vortex shedding from the tower top although this has not been verified.

In the 10 m/s case the blade operates around maximum lift coefficient on most parts of the blade which results in unsteady effects playing an increasing role. There is in the experiment a distinct difference between the aerodynamic response on the inner four span stations and the outer most span station (see Figure 12). The response on the outer section is very similar to the response observed in the 7 m/s case, whereas the response on the three middle sections is characterised by a significant increase in normal force as the blade exits the wake. This clearly indicates that additional mechanisms are at play on the inner parts of the blade. Although the computations do not show exactly the same behaviour the trend is the same with an increased recovery period on the inner parts of the blade. Turning to Figure 19 there is indeed a difference in the flow between the 80% and 95% span sections in that the flow is largely two-dimensional on the outer section whereas trailing edge separation is evident from the 80% span section and inwards. It is likely that the computations did not capture the correct separation points along the blade correctly which would explain the differences in both the freestream level of the normal force as well as the dynamic response to the BWI. The experimental results show that the flow over the blade at the 30% and 47% stations seemingly experiences a change of state as the blade exits the wake. As opposed to the behaviour at the other span stations, this state persists for a relatively large portion of the cycle. This could be connected to the anomalous and highly unsteady flow characteristics at 10 m/s wind speed on this part of the blade which has been identified from both computations and experimental data in previous studies [30, 34]. As can be seen in Figure 12 this behaviour is not reproduced in the present computations. It is also evident from Figure 19 that the vortical structures identified in [30, 34] are not present in the current computations. It was in [?] found that this vortical structure was highly dependent on the inflow velocity and was only identifiable at one wind speed. It is therefore possible that the combination of a slightly different inflow velocity and the presence of the tower upstream of the rotor could cause the structure to not appear. Another likely influence is use of the $k-\omega$ turbulence model, which could have a tendency to suppress such boundary layer structures.

At w=15 m/s (Figure 13) the entire blade operates in the post stall region where the $C_l - \alpha$ curve transitions from a high negative gradient to a fairly low positive gradient on the middle sections of the

blade. There is in the experiment a difference in the blade response between the inner three sections and the outer two sections. On the outer sections the behaviour is similar to that of the middle sections at w=10 m/s, whereas the inner sections do not exhibit this behaviour. Again, there is a disagreement between the experiment and computations of the location of the change in response — however, the qualitative behaviour is similar.

The relatively poor agreement between the computations and experimental results of the normal force at the higher wind speeds (Figures 12 - 13) is most likely due to the high degree of separation which is not accurately captured by the $k-\omega$ turbulence model. It is likely that improvements can be made using the $k-\omega$ SST model since this has previously been shown to give better results at these wind speeds [34]. It also seems that the time constants of the recovery of the blades from the tower shadow at high incidence are too large compared to the experiment, where the recovery to free stream levels is generally faster. In a study on the dynamic stall of the parked NREL Phase VI blade Johansen et al. [15] found that there was little difference between the $k-\omega$ SST model and Detached Eddy Simulation, which both failed to predict the hysteresis loops correctly at high angles of attack. They concluded that this discrepancy could be related to the fact that laminar/turbulent transition was not modelled in these simulations. In the present simulations similar effects could be at play, although the amplitudes of the dynamic stall are much smaller than in [15].

Another important feature of the rotor-tower interaction is the modification of the tower wake structure and shedding frerquency. The loading of the rotor dictates the axial induction, which induces periodic changes in the axial and tangential velocities upstream of the rotor and hence modifies the shedding frequency, phasing and pattern from the tower. In Figure 8 it can be seen that the vortex tubes convect at different velocities along the span of the tower. The vortex shedding is strongly oblique in the region near the edge of the rotor disc. Two mechanisms appear to be at play: one being the difference in axial velocity caused by the rotor induction, and the other the interaction between the tower vortex street with the blade tip vortex, which seems to cause a roll-up and stretching of the tower vortex street. A third mechanism which further influences the phasing and pattern of the shedding is the blade-vortex interaction due to the partial disintegration of the interacting vortices. Additionally, it was observed that the rotation of the rotor wake gave rise to a skewing of the tower wake to one side causing the rotor and tower wakes to interact further downstream causing a greater destabilisation of the turbine wake.

The distinct lack of variation in the blade response and the strong correlation of the tower wake naturally leads one to ask what caused this behaviour. From other aerodynamic applications, most notably the extensive body of work on forced vibration and vortex induced vibration of circular cylinders, it is well-known that vortex shedding from a cylinder can be altered significantly if the structure is subjected to periodic vibration with a forcing frequency that is close to the shedding frequency. The forcing can cause the spanwise correlation of the wake to increase and the frequency and phase of the shedding to be altered. Secondly, it can cause an increase of the shedding strength and mean drag on the cylinder. When the natural frequency of the system and the shedding frequency are sufficiently close to each other the shedding frequency can become synchronised with the forcing frequency. This phenomenon is known as *lock-in*. Lock-in can also occur if the two frequencies are multiples of each other, although the strength of the above mentioned effects become less pronounced. Depending on the amplitude of the forcing the shift of the shedding frequency can be as much as 40%. A detailed review of this subject is given by Blevins [4].

The effect of the downstream rotor on the tower response clearly bears strong resemblances to the characteristics of *vortex lock-in* as described above. The lock-in of the shedding frequency on the blade passage frequency explains the periodicity and spanwise correlation of the blade responses. As discussed above lock-in can occur when the shedding frequency is close to or a multiple of the forcing frequency, which in the low wind case at w=6.7 m/s was 3P and 7P for the 15.2 m/s case. A correlation of the wake also seems to take place when the turbine operates outside the range of lock-in although the effect was not as strong as in the lock-in regime. To substantiate the above arguments further, additional investigations are necessary since at this stage, computations have only been carried out at three wind speeds on one type of wind turbine.

Since there is no data available on the tower forces in the NASA Ames experiment it is not possible to verify whether something similar to this phenomenon also occurred in the experiment. However, from an examination of the blade force responses it was not possible to identify strong periodicity at any of the wind speeds. Likewise, correlation of the blade responses in the spanwise direction were not as strong as in the computations, indicating that the cellular shedding structures were smaller in the experiment than what was found in the computations. One factor which could partly explain the lack of wake correlation and that lock-in was not observed could be that the tower operates in the critical Reynolds number regime where the wake of the tower is highly disorganised due to the transition of the flow in the separation region on the cylinder. The present computations do not take transitional effects into account, which means that the highly unsteady flow characteristics in this regime are not modelled.

The apparent lack of lock-in in the experiment also raises the question whether these findings are purely an artifact of the numerical model or whether indeed this could occur in real-life conditions. It is well-known that the use of Reynolds averaging suppresses small time scales causing structures in the flow to be artificially two-dimensional with large correlation lengths. All structures of small scales in the flow are modelled using an appropriate turbulence model, which particularly for massively separated flows is not always very accurate. LES or hybrid LES models, on the other hand, are capable of reproducing a flow field with three-dimensionally resolved turbulent quantities, which have been shown to predict separated flows more realistically. It is therefore worth investigating whether a more accurate modelling of the small length and time scales of the flow could have an effect on the lock-in phenomenon identified in this work.

The present computations were conducted under very controlled conditions with no background turbulence and a very thin ground shear layer which does not represent realistic atmospheric conditions. An obvious question would be what effect shear and background turbulence have on the vortex shedding on the tower. One might speculate that these factors could cause the vortex lock-in phenomena to occur less frequently, since these are likely to reduce the spanwise correlation lengths of the vortex shedding.

Another important parameter on a downwind turbine, which has not been discussed so far is the blade tower clearance. Its importance is clearly visible in Figures 9 and 10, where the blade passes through the wake in the region where the tower wake vortices are detaching alternately. As such the blade only encounters a single vortex. Had the clearance been slightly smaller, the blade would have passed though the wake in the vortex formation region, which would have most likely resulted in significantly different characteristics of the interaction, where the blade would feel the influence of both the detaching and the developing vortex. A smaller clearance would also be likely to increase the possibility of lock-in phenomena to occur, since the disruption of the vortex formation would be much greater. A further investigation of this parameter is clearly necessary both with respect to its influence on the blade response and the tower response.

In the computations the geometry of the Phase VI turbine was simplified in that, firstly, the rotor was assumed to be non-coned and operating with zero teeter. Secondly, the nacelle was omitted, and finally, the tower was assumed to have a constant diameter along its entire height. The combination of these simplifications could influence the flow over the turbine, since most notably the tower shedding would be altered by the change in tower geometry. Also, a combination of coning and teeter would change the effective incidence of the blade through its cycle, introducing additional dynamic effects. It is therefore the aim in future investigations of the Phase VI turbine to include these features.

One of the major concerns related to downwind turbines is the high levels of low frequency noise (typically in the range of 20-100 Hz) observed to occur occasionally, which cause considerable nuisance to nearby inhabitants. It is generally agreed that these so-called thumping noises are related to the unsteady interaction between the blades and the unsteady wake behind the tower [16, 20, 31]. The large variation in the field measurements indicate that the phenomenon is critically dependent on the exact nature of the interaction. As is evident from the present results as well as the UAE experiment, the highest fluctuations in the blade loading occurred when the blade experienced a direct encounter with a vortex of positive vorticity (type 2). As was shown by Madsen et al. [21], large fluctuations in the pressure distribution on the blade will cause high sound pressure levels, which leads to the conclusion that BVI events are the main contributors to the occasional high levels of low frequently noise.

In field tests of downwind turbines it was found that under certain flow conditions, and more generally during the night, the noise would increase. It seems likely that these events took place in conditions where the shedding frequency coincided with the blade passage frequency making BVI events more frequent. The present results indicate that the rotor causes a spanwise correlation of the vortex shedding to take place. This fact would certainly worsen the effect of a BVI event, because the entire blade would be affected causing the gross pressure fluctuations to be stronger. The additional finding that lock-in could take place on a downwind turbine would cause an increase in the likelyhood of BVI events to occur, as well as increasing the severity of the interaction due to the increase of the vortex intensity. It is thus hypothesised that the present new finding could play

a significant role in the understanding of the acoustic signature of a downwind turbine and should be investigated further both by computational and experimental means.

8 Conclusion

In this article simulations of flow over an isolated rotor and a combined rotor and tower configuration have been presented. For all computations the overset grid version of the EllipSys3D code was used, and it was in Section 5 shown to produce results that were in very good agreement with both the non-overset version of the code and experimental results. The computations carried out on the combined rotor and tower configuration showed that the EllipSys3D solver combined with the newly implemented overset grid method is fully capable of capturing the unsteady interaction between the rotor and tower on a downwind turbine. It was shown that the computations were in reasonably good agreement with the experimental results capturing the key features of the flow that characterise the unsteady interaction. At high wind speeds where the flow was largely separated the agreement with the experiment was less favourable. It can be expected that improvements can be obtained with the use of a different turbulence model as well as an appropriate model for the laminar/turbulent transition. The blade-wake interaction on a downwind turbine is characterised by large fluctuations in the normal and tangential forces of approximately 40% of the freestream level. It was found that unsteady and three-dimensional effects play a significant role in the response of the blades. The pressure distribution was during a BWI event characterised by a large reduction in - and in some cases - a complete collapse of the suction peak on the blade. Interaction with the shed vortices caused significant changes in the pressure distribution on both pressure and suction side. Consequently, it was found that the quarter chord pitching moment varied significantly in nature according to the type of BVI event with up to 30% changes in the moment acting on the blade.

The rotor exerted a significant influence on the tower shedding, affecting shedding frequency, phasing and spanwise correlation of the wake. It was found that under certain flow conditions the tower shedding settled into a state of lock-in, which was driven by the blade passage frequency. These findings do in the opinion of the author warrent further investigation of the nature of the tower response on downwind turbines to gain further understanding of the complexities of rotor-tower interaction.

References

[1] E. Atta. Component-adaptive grid interfacing. In *19th Aerospace Sciences Meeting*, number AIAA-81-0382, St. Louis, MO, January 1981.

[2] E. Barszcz, W. S., and M. R. Dynamic overset grid communication on distributed memory parallel processors. *AIAA paper 93-3311*, 1993.

[3] J. A. Benek, F. C. Dougherty, and P. G. Buning. Chimera: A grid-embedding technique. *AEDC-TR-85-64*, December 1885.

[4] R. D. Blevins. *Flow-Induced Vibration*. Van Nostrand Reinhold Co., New York, 1990.

[5] T. M. Burton and J. K. Eaton. Analysis of a fractional-step method on overset grids. *Journal of Computational Physics*, 137:336–364, 2002.

[6] G. Chesshire and W. D. Henshaw. Composite overlapping meshes for the solution of partial differential equations. *Journal of Computational Physics*, 90:1–64, 1990.

[7] E. P. N. Duque, M. D. Burklund, and W. Johnson. Navier-Stokes and comprehensive analysis performance predictions of the NREL Phase VI experiment. *Solar Energy Engineering*, 125:457–467, 2003.

[8] E. P. N. Duque, C. P. van Dam, and S. C. Hughes. Navier-Stokes simulations of the NREL combined experiment Phase II rotor. *AIAA paper 99-0037*, 1999.

[9] D. Fingersh, D. Simms, M. Hand, D. Jager, J. Cortrell, M. Robinson, S. Schreck, and S. Larwood. Wind tunnel testing of NREL's unsteady aerodynamics experiment. *AIAA paper 2001-0035*, 2001.

[10] W. D. Henshaw. A fourth-order accurate method for the incompressible Navier-Stokes equations on overlapping grids. *Journal of Computational Physics*, 113(1):13–25, 1994.

[11] M. Hinatzu and J. H. Ferziger. Numerical computation of unsteady incompressible flow in complex geometry using a composite multigrid technique. *International Journal for Numerical Methods in Fluids*, 13:971–997, 1991.

[12] B. Hubbard and H.-C. Chen. A chimera scheme for incompressible viscous flows with application to submarine hydrodynamics. In *25th AIAA Fluid Dynamics Confcrence*, number AIAA 94-2210, Colorado Springs, CO, June 20-23 1994.

[13] J. Johansen and N. N. Sørensen. Airfoil characteristics from 3D CFD rotor computations. In *Science of Making Turque from Wind*, pages 9–15, 2004.

[14] J. Johansen, N. N. Sørensen, J. Michelsen, and S. Schreck. Detached-eddy simulation of flow around the NREL Phase-VI rotor. *Wind Energy*, Volume 5(2-3):185 – 197, 16-19 June 2003.

[15] J. Johansen, N. N. Sørensen, J. A. Michelsen, and S. Schreck. Detached-eddy simulation of flow around the NREL Phase VI blade. *Wind Energy*, 5:185–197, 2002.

[16] N. D. Kelly. Acoustic noise generation by the DOE/NASA MOD-1 wind turbine. In *Proceedings of Workshop on Wind Turbine Dynamics*, Cleveland State University, Cleveland, Ohio, 24-26 February 1981.

[17] A. M. Larsen. *Risø Central Computer Facility, Mary*. URL `http://www.risoe.dk/ita/linuxcluster/mary_uk.htm`.

[18] A. Le Pape and J. Lecanu. 3D Navier-Stokes computations of a stall-regulated wind turbine. In *The Science of Making Torque from Wind*, pages 78–88, Delft, The Netherlands, April 2004. EWEA.

[19] J. G. Leishman. Challenges in modeling the unsteady aerodynamics of wind turbines. *Wind Energy*, 5:85–132, 2002.

[20] S. Ljungren. A preliminary assessment of environmental noise from large wecs, based on experiences from swedish prototypes. Technical Report FFA TN 1884-48, FFA, 1984.

[21] H. A. Madsen, J. Johansen, N. N. Sørensen, G. C. Larsen, and M. H. Hansen. Simulation of low frequency noise from a downwind wind turbine rotor. In *Proceedings of the 26th ASME Conference on Wind Energy*, number AIAA-2007-0623, Reno, NV, USA, 8-11 January 2007.

[22] H. A. Madsen, N. N. Sørensen, and S. Schreck. Yaw aerodynamics analyzed with three codes in comparison with experiment. In *Proceedings of 2003 ASME Wind Energy Symposium*, number AIAA-2003-0518, 2003.

[23] R. Meakin. On adaptive refinement and overset structured grids. In *Proceedings of the 13th AIAA Computational Fluid Dynamics Conference*, volume Paper 97-1858, Snowmass, CO, 1997.

[24] R. L. Meakin. A new method for establishing intergrid communication amond systems of overset grids. *AIAA paper 91-1586*, June 1991.

[25] F. R. Menter. Zonal two-equation $k-\omega$ models for aerodynamic flows. *AIAA paper 93-2906*, 1993.

[26] J. A. Michelsen. Basis3D—a platform for development of multiblock PDE solvers. Technical Report AFM 92-05, Technical University of Denmark, 1992.

[27] J. A. Michelsen. Block structured multigrid solution of 2D and 3D elliptic PDEs. Technical report, Technical University of Denmark, 1994.

[28] C. M. Rhie and W. L. Chow. Numerical study of the turbulent flow past an aerofoil with trailing edge separation. *AIAA journal*, 21:1525–1532, 1983.

[29] S. Schreck. The NREL full-scale wind tunnel experiment introduction to the special issue. *Wind Energy*, 5(2-3):77–84, 2002.

[30] S. J. Schreck, N. Sørensen, and M. C. Robinson. Aerodynamic structures and processes in rotationally augmented flow fields. *Journal of Wind Energy*, 10:159–178, 2007.

[31] K. P. Sheppard and H. H. Hubbard. Physical characteristics and perception of low frequency noise from wind turbines. *Journal of Noise Control Engineering*, 1991.

[32] N. N. Sørensen. General purpose flow solver applied to flow over hills. Technical Report Risø-R-827(EN), Risoe National Laboratory, 1995.

[33] N. N. Sørensen. HypGrid2D—a 2-D mesh generator. Technical report, Risø-R-1035(EN), Risoe National Laboratory, 1998.

[34] N. N. Sørensen, J. A. Michelsen, and S. Schreck. Navier-Stokes predictions of the NREL Phase VI rotor in the NASA Ames 80ft $\times$ 120 ft wind tunnel. *Wind Energy*, 5:151–169, 2002.

[35] J. L. Steger, F. C. Dougherty, and J. A. Benek. A chimera grid scheme. In K. N. Ghia and U. Ghia, editors, *Advances in Grid Generation*, volume 5, pages 59–69. ASME FED, 1983.

[36] H. S. Tang. Study on a grid interface algorithm for solutions of incompressible Navier-Stokes equations. *Computers and Fluids*, In Press, 2005.

[37] H. S. Tang, S. C. Jones, and F. Sotiropoulos. An overset-grid method for 3d unsteady incompressible flows. *Journal Of Computational Physics*, 191(2):567–600, 2003.

[38] J. Y. Tu and L. Fuchs. Calculation of flows using three-dimensional overlapping grids and multigrid methods. *International Journal for Numerical Methods in Engineering*, 38:259–282, 1995.

[39] D. C. Wilcox. *Turbulence Modeling for CFD*. DCW Industries, Inc., 2 edition, 1994.

[40] G. Xu. *Computational Studies of Horizontal Axis Wind Turbines*. PhD thesis, Georgia Institute of Technology, May 2001.

[41] G. Xu and L. N. Sankar. Computational study of horizontal axis wind turbines. *AIAA Paper 99-0042*, 1999.

[42] G. Xu and L. N. Sankar. Effects of transition, turbulence and yaw on the performance of horizontal axis wind turbines. *AIAA Paper 2000-0048*, 2000.

[43] F. Zahle. *Wind Turbine Aerodynamics Using an Incompressible Overset Grid Method*. PhD thesis, Imperial College, London, 2006.

[44] Y. Zang and R. L. Street. A composite multigrid method for calculating unsteady incompressible flows in geometrically complex domains. *International Journal of Numerical Methods in Fluids*, 20:341–361, 1995.